AGU PUBLICATIONS

JGR

Journal of Geophysical Research: Oceans

RESEARCH ARTICLE

10.1002/2013JC009388

Special Section:
Early scientific results from the salinity measuring satellites Aquarius/SAC-D and SMOS

Analyzing the 2010–2011 La Niña signature in the tropical Pacific sea surface salinity using in situ data, SMOS observations, and a numerical simulation

Audrey Hasson[1,2], Thierry Delcroix[1], Jacqueline Boutin[3], Raphael Dussin[4], and Joaquim Ballabrera-Poy[5]

[1]LEGOS, UMR 5566, CNES, CNRS, IRD, Université de Toulouse, Toulouse, France, [2]Now at Jet Propulsion Laboratory, California Institute of Technology, Pasadena, California, USA, [3]LOCEAN, UMR 7159, CNRS, UPMC, IRD, MNHN, Paris, France, [4]LEGI, Grenoble, France, [5]ICM/CSIC, Barcelona, Spain

Key Points:
- The well-marked signature of the 2010–2011 La Nina is described and analyzed
- In situ, modeled and SMOS surface salinity products show good overall agreement
- The processes for the western Pacific strong tripolar anomaly shift are studied

Correspondence to:
Audrey Hasson,
Audrey.Hasson@legos.obs-mip.fr

Citation:
Hasson, A., T. Delcroix, J. Boutin, R. Dussin, and J. Ballabrera-Poy (2014), Analyzing the 2010–2011 La Niña signature in the tropical Pacific sea surface salinity using in situ data, SMOS observations, and a numerical simulation, *J. Geophys. Res. Oceans*, *119*, 3855–3867, doi:10.1002/2013JC009388.

Received 30 AUG 2013
Accepted 27 MAY 2014
Accepted article online 3 JUN 2014
Published online 19 JUN 2014

Abstract The tropical Pacific Ocean remained in a La Niña phase from mid-2010 to mid-2012. In this study, the 2010–2011 near-surface salinity signature of ENSO (El Niño-Southern Oscillation) is described and analyzed using a combination of numerical model output, in situ data, and SMOS satellite salinity products. Comparisons of all salinity products show a good agreement between them, with a RMS error of 0.2–0.3 between the thermosalinograph (TSG) and SMOS data and between the TSG and model data. The last 6 months of 2010 are characterized by an unusually strong tripolar anomaly captured by the three salinity products in the western half of the tropical Pacific. A positive SSS anomaly sits north of 10°S (>0.5), a negative tilted anomaly lies between 10°S and 20°S and a positive one south of 20°S. In 2011, anomalies shift south and amplify up to 0.8, except for the one south of 20°S. Equatorial SSS changes are mainly the result of anomalous zonal advection, resulting in negative anomalies during El Niño (early 2010), and positive ones thereafter during La Niña. The mean seasonal and interannual poleward drift exports those anomalies toward the south in the southern hemisphere, resulting in the aforementioned tripolar anomaly. The vertical salinity flux at the bottom of the mixed layer tends to resist the surface salinity changes. The observed basin-scale La Niña SSS signal is then compared with the historical 1998–1999 La Niña event using both observations and modeling.

1. Introduction

The El Niño Southern Oscillation (ENSO) phenomenon is the strongest climatic signal on Earth at the interannual time scale. Even though it originates in the tropical Pacific Ocean, ENSO has global environmental impacts through the modification of the atmospheric circulation via teleconnections [e.g., *Trenberth et al*., 1998]. These changes affect for instance precipitation in the tropical Pacific [*Ropelewski and Halpert*, 1996], in Northern America [*Cole et al*., 2002], in Africa [*Nicholson and Selato*, 2000], and in Southeast Asia [*Kripalani and Kulkarni*, 1997]. ENSO comprises the most-studied warm El Niño phase as well as the less-documented cold La Niña phase [*Philander*, 1985]. These two phases, respectively, correspond to warmer and colder-than-usual Sea Surface Temperature (SST) in the eastern-central equatorial Pacific. Details about ENSO main features and mechanisms can be found in several textbooks, including those of *Philander* [1989], *Clarke* [2008], and *Sarachik and Cane* [2010] to name a few.

Measurements of salinity have been performed since the late 17th century. Salinity remains however not as well sampled as temperature. The broad-scale Sea Surface Salinity (SSS) variability is relatively well known at the seasonal and (ENSO) interannual time scales in the tropical Pacific Ocean owing to ship of opportunity and TAO/TRITON moorings measurements. A recent overview of the SSS ENSO signature was presented in the Introduction section of *Hasson et al*. [2013a]. The ENSO signature in SSS is mainly located in the western half of the tropical Pacific Ocean, with lower-than-normal salinity waters in the equatorial band and higher-than-normal values along the mean position of the South Pacific Convergence Zone (SPCZ) during El Niño events. To the first order, the opposite anomaly occurs during La Niña events [*Delcroix and Hénin*, 1991; *Gouriou and Delcroix*, 2002]. The SSS ENSO signal amplitude is of the order of 1 pss, which is twice the seasonal SSS signal [see *Delcroix*, 1998]. In contrast to SSS, most of the main SST ENSO signature is located in the eastern half of the basin, trapped in the equatorial band [*Rasmusson and Carpenter*, 1982, *Vialard et al*., 2001].

© 2014. American Geophysical Union. All Rights Reserved.

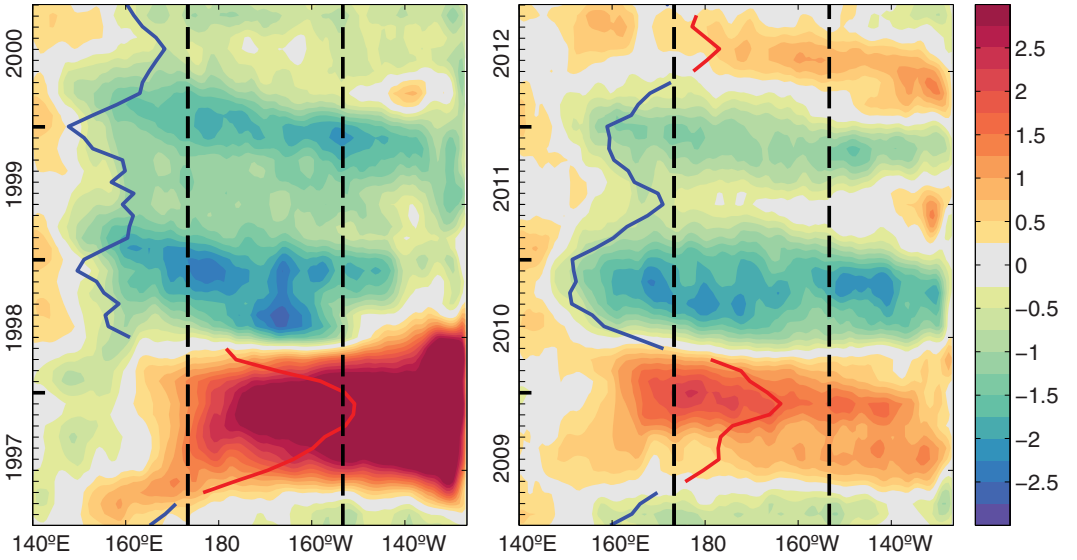

Figure 1. Longitude-time plot of the monthly SST anomaly (°C) averaged between 2°S and 2°N from (a) 1997 to 2000 and (b) 2009 to 2012, SST anomalies are relative to 1982–2012. The solid line represents the Niño 3.4 SSTA (ENSO index) centered on 170°E (20° of longitude correspond to 1°C in SSTA). When blue, the line represents negative SSTA (La Niña phase) and when red, positive SSTA (El Niño phase). The dashed lines represent the longitudinal zone within which the NIÑO 3.4 index is computed.

The main mechanisms responsible for La Niña-related SSS changes are qualitatively well described [*Delcroix and Picaut*, 1998; *Vialard et al*., 1998a, 1998b; *Picaut et al*., 2001; *Gouriou and Delcroix*, 2002; *Vialard*, 2002; *Singh et al*., 2011; *Hasson et al*., 2013a] and are summarized as follows. During La Niña the Trade Winds intensify over the Pacific Ocean, reinforce the equatorial upwelling and affect SSS east of the dateline along the equator by bringing high-salinity waters from below. The enhanced Trade Winds also generate equatorial upwelling Kelvin and downwelling Rossby waves whose associated westward current anomalies in the equatorial band lead to the westward displacement of the warm and fresh waters of the warm pool. Surface mean currents are also modified away from the equatorial band during La Niña. Changes in the western Pacific SSS are linked to the intensification of the southern branch of the westward South Equatorial Current (SEC) and the eastward North and South Equatorial Counter Currents (NECC, SECC). Moreover, the warm pool westward displacements shift the ascending branch of the Walker circulation and associated heavy precipitation to the west. In consequence, the far western Pacific SSS decreases whereas the western-central equatorial region SSS increases. In the south-western tropical Pacific, the SPCZ is shifted south to its mean position where SSS is modified by the coincident related heavy precipitation regime. Meridional advection also contributes to SSS changes within 3°S and 6°S.

Aside from analyzing the ENSO signature in terms of SSS, various studies have shown the important role of salinity in ocean dynamics in the tropical Pacific [e.g., *Vialard and Delecluse*, 1998; *Vialard et al*., 2002]. In the western tropical Pacific Ocean, salinity stratification in the upper ocean can lead to the formation of barrier layers. Barrier layers occur when the salinity mixed layer depth is shallower than the temperature mixed layer depth and therefore salinity stratification controls the density mixed layer depth. The induced shallow density mixed layer shuts down entrainment cooling and enhances local response to wind stress by trapping air-sea momentum fluxes in a thinner layer. Salinity stratification can therefore modulate air-sea interactions involved in ENSO dynamics [*Lukas and Lindstrom*, 1991]. *Maes et al*. [2002] used a coupled model to show the importance of the salinity-related barrier layer to set up the ocean state prior to an El Niño event. While the barrier layer thickness cannot directly be detected by surface only measurements, there is evidence of a link between barrier layer thickness, SST anomalies and SSS horizontal gradient in the western Pacific warm pool [e.g., *Delcroix and McPhaden*, 2002; *Bosc et al*., 2009].

Following the strong 2009 El Niño event, the tropical Pacific Ocean rapidly turned into a strong La Niña mid-2010 [*Kim et al*., 2011]. This La Niña phase has lasted for about 2 years with two periods of maximum negative equatorial SST anomalies, occurring during the boreal falls of 2010 and 2011 (Figure 1b), nearly in

© 2014. American Geophysical Union. All Rights Reserved.

phase with the mean seasonal SST cooling. For the first time, the Soil Moisture/Ocean Salinity (SMOS) mission provides satellite observations of SSS over the World Ocean [*Kerr et al*., 2010; *Font et al*., 2010], and thus basin-wide SSS observations of the tropical Pacific Ocean in its La Niña phase. Taking advantage of such an unprecedented satellite data set, but also combining in situ and model data sets, this study aims at describing and analyzing the 2010–2011 La Niña signature in SSS.

This paper is organized as follows. Data and methodology are described in section 2. We then intercompare the SMOS, in situ, and model data sets. The 2010–2011 La Niña phase is subsequently described in section 3 in terms of SSS, based on all data sets. The SSS variability and related mechanisms are assessed in section 4, using the model only to identify processes behind the observed changes. A comparison with the historical 1998–1999 La Niña is done in section 5; discussion and conclusions are given in the section 6.

2. Data and Methods

2.1. Data Description

Our analysis is carried out using complementary SMOS, in situ, and model-derived near-surface salinity data sets. SMOS was launched in November 2009 and started delivering data a few months later. Several SSS products are available at the *Centre Aval de Traitement de Données* SMOS (CATDS) at different time and space resolutions and with different correction approaches. The SMOS SSS data that we use come from the CATDS CEC-LOCEAN v2013 product built using ascending and descending SMOS passes. This product is created from the European Space Agency (ESA) level 2 data without any adjustment to climatology other than a mean bias correction (the so-called Ocean Target Transformation estimated in the south east Pacific Ocean as described in *Yin et al*. [2013], preserving the SSS interannual variability estimated by the satellite. The SSS are gridded over a $0.25^\circ \times 0.25^\circ$ grid, every month, from January 2010 to December 2012, using a running average over 100×100 km^2. Data during the commissioning phase (January to June 2010) must be interpreted with care as the calibration control parameters of the instrument were quite variable, which is not the case since June 2010 [*Boutin et al*., 2012]. Data are made freely available by the CATDS on the expertise center webpage (see Acknowledgements for all data sets web addresses).

Salinity measurements from thermosalinographs (TSG) have been obtained from 1991 until present from the Voluntary Observing Ships (VOS) programs of the French SSS Observations Service. We will especially focus on data collected along the shipping routes from New Caledonia to Kiribati, as they cross the region of maximum ENSO-related SSS variability (see below). They correspond to three different VOS: Coral Islander 2, Pacific Islander 2, and Tropical Islander. SSS are measured every 15 s and median values over 5 min are stored. Because of the ships' draught and average speed (20 knots), the measurements are thought to represent an average of the first 10 m depth and have an average of 3 km along track resolution [*Hénin and Grelet*, 1996]. In this study, the horizontal resolution is degraded to 30 km (i.e., averaging over 10–11 data points) to allow for better comparison with other data sets. The SSS is processed by a quality control algorithm involving comparison with climatology, daily bucket samples collected on board and collocated near-surface Argo data. The accuracy of SSS values (of the order of 0.02 globally) is a function of the linear-fit adjustment between TSG versus bucket samples and collocated Argo measurements (G. Alory, personal communication, 2013). Only "Good" and "Probably Good" flagged data were kept for our study.

The Argo profiling float network is being deployed to sample the World Ocean since about 2002 [*Roemmich and Owens*, 2000]. The ISAS (In Situ Analysis System) univariate objective analysis (OA) is based on the data provided by Argo and, to a lesser extent, on complementary data such as TAO-TRITON moorings and CTD casts in the tropical Pacific [*Gaillard et al*., 2009]. We use here the 6th version of ISAS on a global $1/2^\circ \times 1/2^\circ$ horizontal mesh (77°S–66.5°N) released in early 2013 with monthly data from 2002 to 2011. The Argo temperature and salinity profiles are first interpolated to standard depths. The OA method is then used to spatially interpolate temperature and salinity fields at each horizontal and temporal grid point. Around each grid point, only data included in a three-dimensional ellipsoid defined by $L_x = 600$ km of longitude, $L_y = 300$ km of latitude and $L_t = 3$ weeks are kept in the analysis. Covariance scales are 300 km wide in longitude, proportional to the Rossby radius of deformation in latitude, and 3 weeks long in time. The accuracy of the objectively analyzed T and S gridded values thus depends on the number of nearby data. If there is no observation within the ellipsoid then the output data corresponds to a first guess climatological seasonal cycle derived from a previous ISAS analysis. Temperature, salinity, and associated errors are available from

© 2014. American Geophysical Union. All Rights Reserved.

the surface to a depth of 2000 m. We average the first four vertical levels within 0–10 m to represent SSS for the purpose of this study. Only data with associated error below 80% were kept in our study (using slightly different percentage values did not qualitatively change our results). Details can be found in *Gaillard et al.* [2009] and in a dedicated technical report [*Gaillard et al.*, 2012].

The SST fields used here (in Figure 1) are derived from an optimal interpolation of both in situ and satellite data [*Reynolds et al.*, 2002]. This data set is produced by the National Oceanic and Atmospheric Administration (NOAA) and is available weekly from November 1981 to present on a $1^\circ \times 1^\circ$ grid.

The numerical simulation was run by the DRAKKAR group based on the 3.2.1 version of the NEMO ocean general circulation model code [*Madec*, 2008]. Our specific model run (ORCA025.L75-MRD911) has been forced by a modified ERA-interim reanalysis to prevent direct SSS restoring (usually performed to avoid long-term salinity drift) so as to preserve SSS interannual variability [see *Hasson et al.*, 2013a]. The simulation is available from 1990 to 2011 on a $0.25^\circ \times 0.25^\circ$ horizontal resolution and with 75 vertical z-coordinate levels. The model time step is 960 s and outputs are archived every five simulated days. There are eight levels between the sea-air interface and 10 m depth. Their average will be referred to as *surface* data in the present study. Model data are routinely evaluated against dedicated metrics by the DRAKKAR group, and outputs within the mixed layer have been further assessed in *Hasson et al.* [2013a, 2013b]. Comparisons against in situ observations have highlighted the model ability to reproduce near-surface salinity variability at various time scales. The model showed a particularly good representation of the fresh pool zonal displacements during ENSO events in the equatorial band. Following the methodology developed by *Vialard et al.* [2002], all terms responsible for the mixed layer salinity (hereafter called SSS) variability are computed at each model original time step (and then archived every 5 days). These online computations enable us to precisely quantify mechanisms involved in the mixed-layer salinity budget equation (more details in section 4).

2.2. Data Assessment

In this section, all products described above are assessed through their mutual comparison, bearing in mind their different horizontal and time resolutions, as well as the diverse optimal interpolation methods. Moreover, one should notice that the term "SSS" does not account for the same layer depth in all data sets. SSS refers to the 0–10 m average salinity for all data sets except for the satellite based ones, as SMOS SSS corresponds to the ocean top centimeter. SSS derived from SMOS data indeed corresponds to the ocean top first centimeter. During localized heavy rain events dissimilarities have been observed in near-surface salinity data from different data sets and therefore different depths [*Hénocq et al.*, 2010; *Boutin et al.*, 2013]. Although our study focuses on large-scale dynamics and on long time scales, we analyze regions of heavy precipitation (such as the fresh pool and the intertropical convergence zones). However, when looking at monthly estimates in the region under study, this effect is expected to remain less than 0.1 when considering a linear dependency of 0.16 pss $(\text{mm hr}^{-1})^{-1}$ between salinity and quasi-instantaneous rain rate [*Boutin et al.*, 2013]. Satellite monthly mean rain rates are most of the time less than 0.8 mm hr^{-1} in the region. We can thus expect SMOS data to be slightly freshly biased as compared to the other salinity data sets.

The SSS time average and standard deviation of the monthly ISAS data set over the 2010–2011 period are shown in Figures 2a and 2b. To allow better comparison, the average and standard deviation anomalies relative to ISAS are shown for the model and SMOS (Figures 2b, 2c, 2e, and 2f). We are restricting here our investigation to the western half (140°E–140°W; 25°S–10°N) of the tropical Pacific where the maximum SSS interannual variability is observed [*Hasson et al.*, 2013b]. On the large scale, the modeled, ISAS, and SMOS fields are consistent. For the mean fields, the SSS spatial correlation coefficients are 0.97 between ISAS and the numerical simulation, and 0.87 between ISAS and SMOS values, with RMS errors of 0.26 and 0.34, respectively. All data sets portray the "low SSS-high variability" region, roughly west of 170°W, linked to the SPCZ and fresh pool positions, and the "high SSS-low variability" to the east of 170°W in the Southern Hemisphere. Even though the overall mean patterns are well reproduced, the model simulates lower-than-observed SSS in the low SSS regions and higher-than-observed in the high SSS regions [see *Hasson et al.*, 2013a, 2013b, for details]. The model also produces stronger SSS variability in the high-variability region than SMOS and ISAS. Large biases can especially be found in the mean and standard deviation fields between Fiji and Vanuatu (Figures 2c and 2f). It is however hard to say to what extent these differences are due to the model or to the objective analysis expected smoothed variability in the observed fields. One can also find large local biases in the mean and standard deviation fields near coastlines and Pacific Islands in

© 2014. American Geophysical Union. All Rights Reserved.

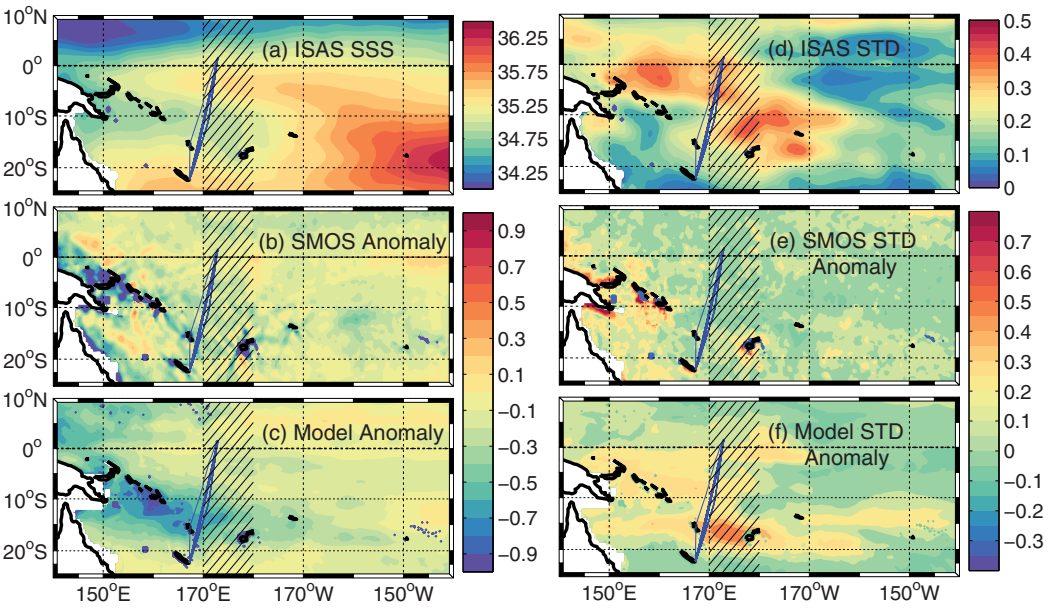

Figure 2. The 2010–2011 averaged Sea Surface Salinity (pss) in the western tropical Pacific from (a) ISAS and (d) its associated standard deviations over the same period. Anomalies with respect to ISAS of the (b) SMOS and (c) modeled SSS fields and of the (e and f) respective standard deviations. Blue lines represent the VOS routes discussed in Figure 3 and the 170°E-180° hatched zones the computation area of Figures 5–7.

SMOS data set (Figures 2b and 2e). They could be due to radio frequency interferences (RFI) disturbances coming from sources located on the islands or vessels. RFI are imperfectly sorted out by the ESA v5 processing. The analysis of RFI (not shown here) actually shows frequent occurrences around the Fiji, Solomon and Tuvalu Islands. The observed large biases could also reveal flaws in the image reconstruction linked with the presence of land in the SMOS field of view, as evidenced around large landmasses by previous studies [e.g., *Vergely et al.*, 2013].

The modeled, SMOS, and ISAS SSS data sets are also compared to the high-resolution (30 km) TSG values. To do so, the model output and SMOS data are averaged on a 100 km radius centered on each TSG data point, using a 10 and 9 day window, respectively. The ISAS data set is collocated onto the TSG data using a 1 month window and within a 50 km radius. (Recall that the original model and ISAS time resolutions are 5 days and 1 month, respectively, and that the near-repeat cycle of SMOS is 18 days.) Collocations with less than 30 SMOS measurements are discarded. A total of 16 VOS tracks crossing the SSS high-variability region while sailing between New Caledonia and Kiribati have been selected for the comparison (blue lines in Figure 2). Figure 3 shows the TSG SSS along two representative tracks in July 2010 and 2011 and collocated SSS from the three other data sets. On the one hand, ISAS and TSG compare rather well with a SSS minimum of the same amplitude and position. As expected, ISAS does not reproduce small-scale variability because of its 1 month resolution and its optimal interpolation method described above. One must however keep in mind that the Argo data used for ISAS were partly considered during the TSG quality control procedures. Even though TSG and ISAS are not strictly independent products, this comparison shows that ISAS performs well at reproducing the large-scale SSS variations captured by TSG. On the other hand, SMOS and the model have a fresh bias when compared to the other two data sets south of about 8°S. For these particular transects, the mean difference from the TSG data is −0.18 and −0.38 for SMOS and the model respectively. As stated above, lower than observed (in situ) SSS derived from SMOS in the SPCZ region could be partly explained by the effect of heavy precipitation on the satellite salinity retrieval [*Boutin et al.*, 2013]. The large (about 0.5) underestimation of SMOS SSS with respect to TSG SSS south 10°S in 2011 is however most probably an artifact from RFI as mentioned earlier. The position of the SSS minimum is nevertheless well reproduced by all data sets. They all show a shift of the relative SSS minimum from about 8°S–10°S in July 2010 to 14°S–16°S in July 2011.

Statistics for all tracks are of the same order of magnitude and can be found in Table 1. They are of poorer quality than the ones found in the eastern Pacific Ocean (mean difference of −0.07 and standard deviation

© 2014. American Geophysical Union. All Rights Reserved.

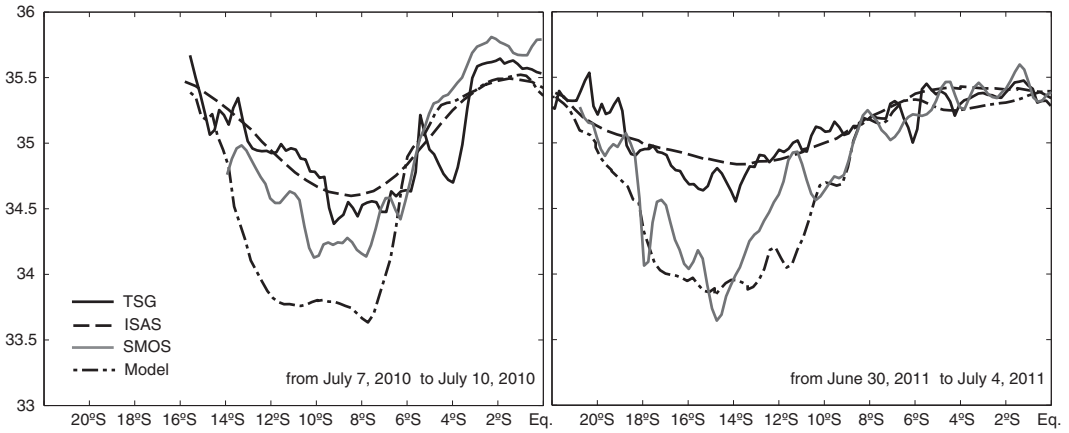

Figure 3. VOS-TSG SSS (solid black) collected along the VOS routes shown in Figure 2 and colocated ISAS (dashed), SMOS (solid gray), and model (dot-dashed) SSS in (left) July 2010 and (right) July 2011. All in pss.

of the difference of 0.20 in *Hasson et al*. [2013a]) likely because of RFI and landmasses pollution. Restricting the comparison north of 10°S, RMS errors decrease by over 10% and mean differences are below 0.2. Regarding SMOS and ISAS, it is interesting to note that our statistics compare well with what was found when comparing SMOS with Argo data (last row of Table 1) in the Pacific ITCZ region [*Boutin et al*., 2013].

3. The 2010–2011 ENSO Signature in SSS

Figure 4 shows the July 2010 and July 2011 SSS anomalies relative to the 2010–2011 period for each three gridded products. The month of July has been chosen as it is the first month after the SMOS commissioning phase. Spatiotemporal variability of the broad structures produced by the three products is in good agreement with one another, even though there are discrepancies at the smaller scale and in the amplitude (similarly as in Figures 2 and 3). Small structures observed by SMOS can indeed not be reproduced by ISAS construction. In July 2010, a large negative SSS anomaly of the order of −0.5 stretches from the Solomon to French Polynesia islands within about 5°S and 15°S. This anomaly is bracketed by two positive anomalies of the order of +0.5 to the north between 5°S and 5°N and to the south between 25°S and 15°S (Figures 4a–4c). Most of these SSS anomalies have drastically reversed signs 1 year later, in July 2011 (Figures 4d–4f). These changes are consistent with the location of the maximum standard deviation in Figure 2 (right) as well as with the southward 5–10° latitude shift of the minimum SSS values between July 2010 and July 2011 in Figure 3.

The latitude-time plots of the SSS anomaly relative to the 2010–2011 period derived from each three SSS products averaged within the 170°–180°E band (hatched area on Figures 2 and 4) are shown in Figures 5a–5c. One can observe the concurrent timing and latitudinal shift positioning of the positive and negative SSS anomalies. These anomalies seem to be following the NIÑO3.4 SST index (solid red and blue lines in Figure 5). In early 2010, during the 2009–2010 El Niño wrap-up, a strong negative SSS anomaly (over −0.8) spans from 10°S to 10°N, and a positive SSS anomaly (over +0.8) appears south of 8°S. During the following late

Table 1. Comparison of Along Track TSG SSS (Blue Lines in Figure 2) With Collocated SMOS, ISAS, Modeled SSS[a]

Data Sets to be Compared	Mean Differences (pss)	Standard Deviation of the Differences (pss)	RMSE (pss)	N
TSG-SMOS	0.21	0.27	0.33	1508
TSG-ISAS	−0.01	0.18	0.18	1698
TSG-Model	0.28	0.36	0.46	1698
SMOS and Argo	0.23	0.35	0.42	692

[a]Last row is a comparison of SMOS SSS and collocated Argo SSS in the ITCZ region (5°N–15°N; 180°W–110°W) from *Boutin et al*. [2013]; note that the latter uses a temporal radius of colocation of 10 days that leads to a slightly higher RMSE than in the present study. N corresponds to the number of comparison data point.

© 2014. American Geophysical Union. All Rights Reserved.

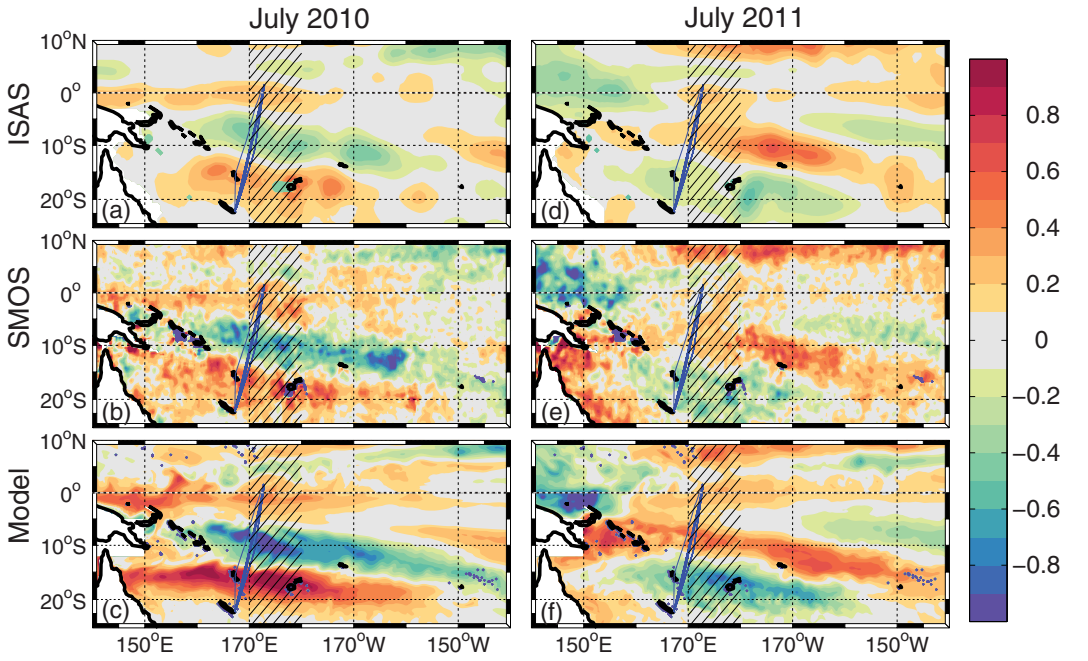

Figure 4. SSS anomalies relative to each product 2010–2011 monthly climatology (pss) in (left) July 2010 and (right) July 2011 for (a and d) ISAS, (b and e) SMOS, and (c and f) the model. Hatched zones and blue lines are identical to Figure 2.

2010 La Niña episode the various data sets show a strong triplet of anomalies, positive north of 10°S, negative within about 10°S and 18°S, and then positive again south of 18°S. In 2011, the negative anomaly shifts southward and becomes stronger as does the northern positive anomaly. This ENSO evolution is consistent with the analysis of *Delcroix and Hénin* [1991] based on the 1969–1988 VOS bucket data available at that time. Authors underlined the co-occurrence of regional changes in SSS and in precipitation due to the ENSO effect on the Walker circulation. They however recall their earlier study [*Delcroix and Hénin*, 1989] that stated the possible important role of mixing and advection upon the 1982–1983 ENSO SSS changes in the SPCZ region. The following section presents an assessment of the role of each process in the salinity variability, as reproduced by the model.

4. Mechanisms Associated With the 2010–2011 SSS Anomalies

In order to understand the 2010–2011 variations in SSS, we investigate the processes that modify salinity within the mixed layer (hereafter still called SSS), using an approach based on our model outputs as in *Hasson et al.* [2013a] and earlier with other models in *Vialard and Delecluse* [1998a, 1998b] and *Vialard et al.* [2002].

The equation of the SSS budget may be written as

$$\underbrace{\partial_t \langle S \rangle}_{I} = \underbrace{\frac{(E-P-R)}{H} \cdot \langle S \rangle}_{II} - \underbrace{\langle \vec{u}_h \cdot \vec{\nabla}_h S \rangle}_{III} + \underbrace{\frac{(w_e + d_t H) \cdot \delta S}{H}}_{IV} - \underbrace{\langle \vec{\nabla}_h \left(K_h \cdot \vec{\nabla}_h S \right) \rangle}_{V} + \underbrace{\frac{\partial_z (K_z \cdot \delta S)}{H}}_{VI} \quad (1)$$

Where $\langle X \rangle = \frac{1}{H} \int_{-H}^{0} X(z) dz$ corresponds to the parameter X averaged within the mixed layer of depth H defined with a 0.01 kg m^{-3} density criteria. The other parameters are referred to as follows: E for the evaporation, P for the precipitation, R for the river runoff (∼0 in our study domain), u_h for the horizontal velocity (including both zonal u and meridional v), w_e for the entrainment velocity, and K for the diffusion coefficient (horizontal (K_h) and vertical (K_z)). Moreover, δS denotes the salinity jump at the base of the mixed layer. Term (I) will be referred to as the SSS tendency and term (II) as the surface forcing. Terms (III) and (V) are, respectively, the horizontal advection and diffusion processes. Analogously, terms (IV) and (VI) are the vertical advection and entrainment and the subscale vertical processes. For conciseness, terms (III) and (V) are

© 2014. American Geophysical Union. All Rights Reserved.

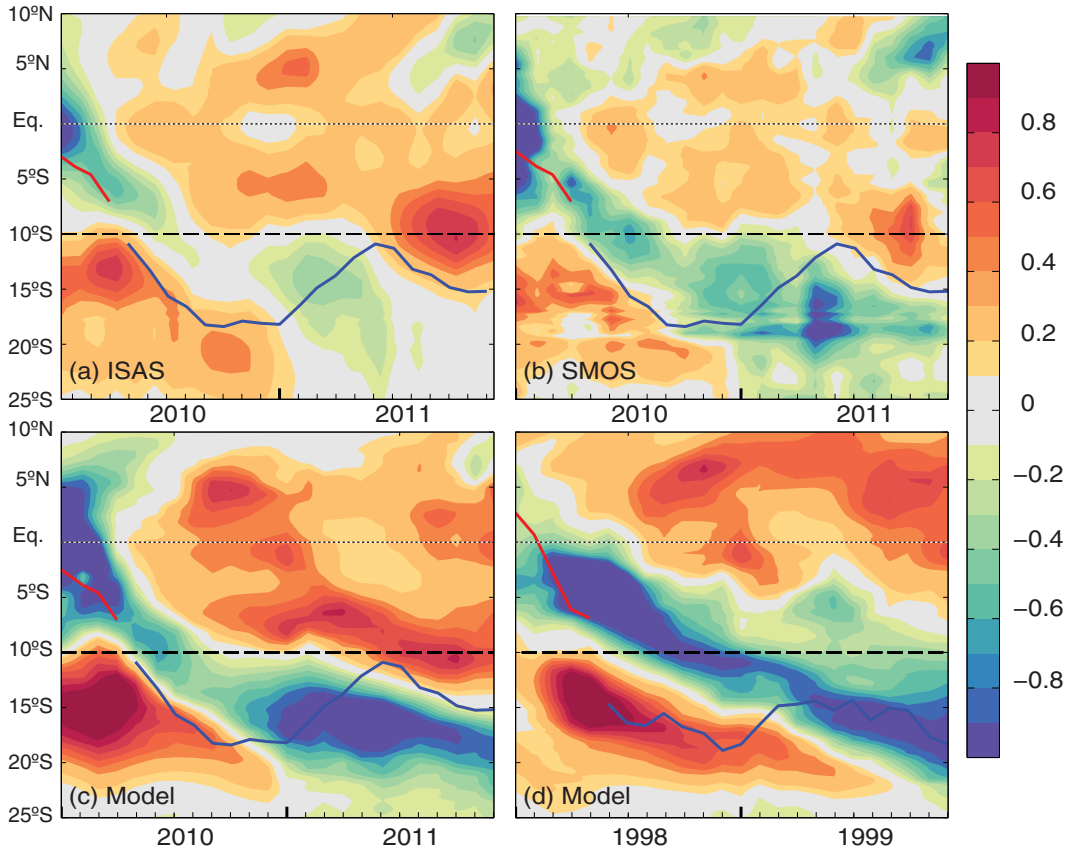

Figure 5. The 2010–2011 latitude-time plot of the 170°E–180°E averaged SSS anomalies (pss) from (a) ISAS, (b) SMOS, and (c) the model. (d) Analogous plot from model data over the 1998–1999 period. The solid line is the Niño 3.4 SSTA (equivalent to Figure 1 but centerd on 10°S dashed line (with 20° of latitude corresponding to 1°C in SSTA).

denominated together as the horizontal advection, and terms (IV) and (VI) together as the vertical salt flux through the mixed layer base (will be hereafter called subsurface forcing).

As described above, the numerical simulation computes, at every model time step, all terms of the equation but the entrainment one. The last has been found to be rather insignificant as the other terms balance well enough. Terms computed at every model time step are called hereafter "online computed." Any computation done with the state variables 5 day archive, such as u, v, S, T, is referred to as "offline." Figures 6a–6d show the latitude-time plots of the interannual SSS tendency and of the three interannual forcing terms averaged within 170°E–180°E (as in Figure 5). The data shown in Figure 6 are the anomalies from the respective monthly climatology of the various budget components (as an example, for zonal advection, that would be $u \cdot S_x - \overline{u \cdot S_x}$ following the definition of equation (2) below). Monthly climatologies are computed from the model outputs using a 25 month Hanning filter to screen out the possible effect of ENSO influence and then averaged month by month (similarly as in *Hasson et al.* [2013a, 2013b]).

A positive anomaly in SSS tendency of the order of $+5$ pss yr^{-1} stretches from about 5°N in early 2010 to 8°S in mid-2010 (Figure 6a), and a negative anomaly of similar amplitude spans from about March to December 2010 between 7°S and 20°S. As expected, these two events are consistent with the SSS changes portrayed by Figure 5. During these two events, the horizontal advection (Figure 6b) seems to be the main driver of SSS changes. The respective contribution of the online-computed interannual zonal and meridonal salt advection components are shown on Figures 7a and 7b. It reveals that the zonal advection is the main actor of the SSS changes in the equatorial band, whereas meridional advection dominates SSS changes processes further south. The zonal and meridional advections were further analyzed by splitting the impact of the mean seasonal currents and salinity field and the interannual ones. The zonal advection can be divided as:

© 2014. American Geophysical Union. All Rights Reserved.

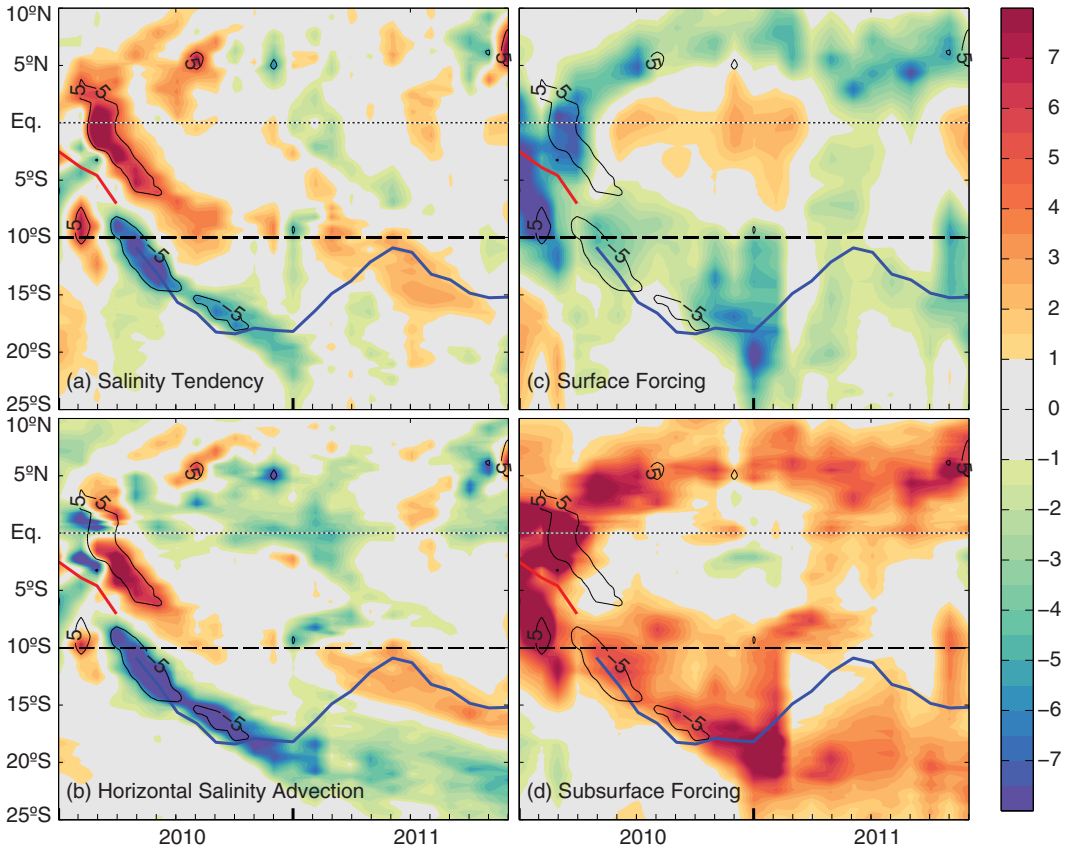

Figure 6. The 2010–2011 latitude-time plot of the 170°E–180°E interannual modeled (a) SSS tendency, (b) horizontal SSS advection, (c) surface and (d) subsurface forcing. The 5 and −5 pss yr^{-1} contour of the salinity tendency is superimposed on all plots. The solid colored line is identical to the one on Figure 5. Unit is pss yr^{-1}.

$$u \cdot S_x = (\bar{u} + u') \cdot (\bar{S}_x + S'_x)$$
$$= \underbrace{\bar{u} \cdot \bar{S}_x}_{I} + \underbrace{\bar{u} \cdot S'_x}_{II} + \underbrace{u' \cdot \bar{S}_x}_{III} + \underbrace{u' \cdot S'_x}_{IV} \quad (2)$$

Where $\bar{X}$ denotes the mean seasonal component and X' the relative interannual variability. Meridional advection can be decomposed in an analogous manner. The mean seasonal advection of interannual salinity anomalies (II), the interannual anomalous advection of mean seasonal salinity fields (III), and the interannual advection of the interannual salinity fields (IV) are shown in both zonal and meridional directions on Figures 7c–7h. These terms are computed "off-line," i.e. with 5 day archived modeled currents and salinity outputs. Even though "off-line" calculation is not exact because they cannot catch variability in time scales smaller than 10 days, it gives informative insights of the processes at work. Since this study focuses on changes at the interannual scale, the mean seasonal advection of the mean seasonal salinity field (I) will not be presented.

As mentioned above, the greatest zonal advection signal is found in the equatorial band, especially during the El Niño-La Niña transition phase (Figure 7a), which is characterized by significant changes in the SSS (Figure 6a). Zonal salinity advection is mainly driven by interannual changes in the salinity zonal gradient linked to the preceding El Niño within 5° off the equator advected by both the mean zonal (Figure 7e) and the interannual currents (Figure 7g). Negative zonal salinity advection can also be noticed around 5°N (Figure 7a), which can be linked to the eastward intensification of the NECC. It is roughly counterbalanced by meridional advection (Figure 7b). Meridional salinity advection is the strongest in the Southern Hemisphere during 2010 and early 2011(Figure 7b), most of which can be explained by the advection of interannual anomalous meridional salinity gradient (Figures 7f and 7h). The interannual modulation of the meridional currents (that can be linked to the ENSO variability of the trade winds) only weakly impacts SSS (Figure 7d).

© 2014. American Geophysical Union. All Rights Reserved.

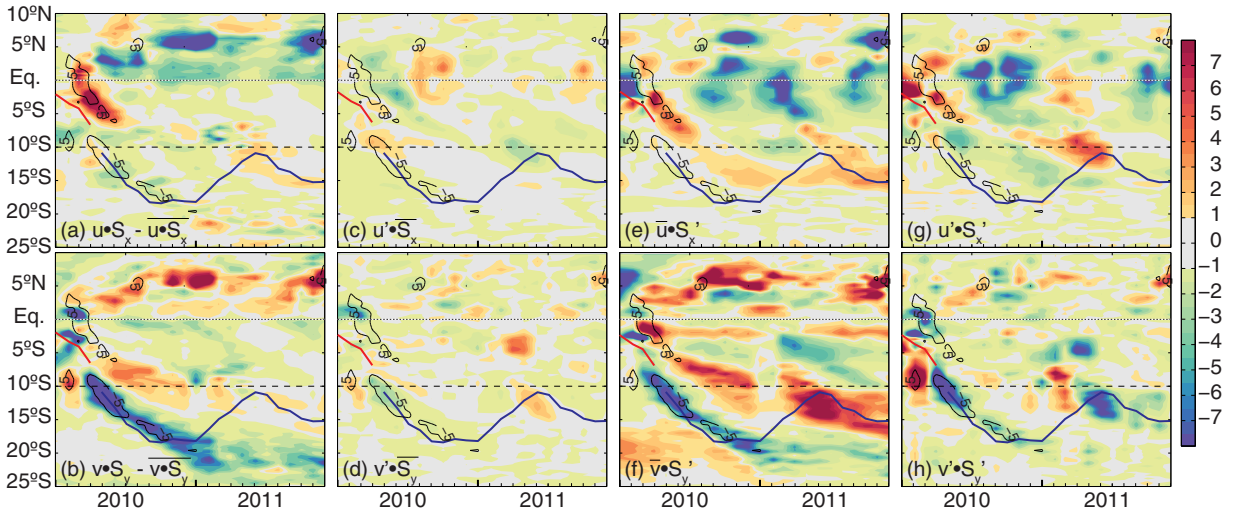

Figure 7. The 2010–2011 latitude-time plot of the 170°E–180°E (top) decomposed zonal and (bottom) meridonal salinity advection in pss/yr. (a and b) Online-computed interannual components. Off-line computed (from 5 day modeled outputs) advection of (c and d) mean seasonal salinity gradients by interannual currents, (e and f) interannual salinity gradients by mean seasonal currents, and (g and h) interannual salinity gradients by interannual currents. The advection of mean seasonal salinity gradients by mean seasonal currents is not shown. The lines are identical to the ones on Figure 5.

Salinity anomalies set up at the equator by zonal advection of the warm/fresh pool due to El Niño. This results in early 2010 in an increase of both the equatorial zonal and the 10°S meridional SSS gradients (Figure 5c). By mid-2010, there is an important bipolar meridional gradient anomaly, positive between the equator and 10°S and negative from 10°S to 17°S. They are then exported southward by the mean and interannual poleward currents in the Southern Hemisphere (Figures 7f and 7h).

Figure 6c shows a negative anomaly of surface forcing between 5°N and 10°S in early 2010, with values below -5 pss yr^{-1} enhancing the negative SSS tendency. Examination of the off-line P and E modeled fields indicates that this surface forcing term is mainly modulated by the strongly dominant P (not shown). By mid-2010, the La Niña phase develops and the equatorial surface forcing anomaly changes from negative to positive. A north-south dipole of surface forcing is in place from mid-2010 to mid-2011 in each hemisphere. The surface forcing positive anomaly near the equator faces negative anomalies south of 10°S and north of 5°N. The positive anomaly (i.e., decrease of P) is linked to the La Niña induced westward shift out of our domain of the ascending branch of the Walker circulation. The negative anomaly south of about 10°S (i.e., increase of P) is due to the enhanced activity of the SPCZ during La Niña. As described in *Hasson et al.* [2013a] for a different time period, the subsurface forcing has a damping effect on SSS changes. Vertical mixing is enhanced because of the strengthening of the vertical S gradient (Figure 6d). Subsurface processes also damp the effect of horizontal advection away from the equatorial band but to a lesser extent. Vertical processes progressively erode the SSS anomaly as it shifts southward. This is probably the main process that limits the southward expansion of the La Niña induced anomalies. This is however out of the scope of the present study. Moreover, one must keep in mind that vertical mixing is parametrized in the model and should be interpreted with care.

5. Comparison With the 1998–1999 La Niña

This section underlines similarities and dissimilarities between the 1998–1999 and the 2010–2011 La Niña events in terms of SSS changes and driving mechanisms. The 1998–1999 La Niña event followed an extremely strong El Niño event that lasted from early 1997 to mid-1998 (Figure 1a). Observations and models indicate that the 1997–1998 El Niño event was characterized by equatorial waters fresher than 35 pss extending unusually far from the mean fresh pool position to the American coast, chiefly driven by horizontal advection to the west of 160°W and surface forcing to the east [*Vialard et al*, 2002; *Hasson et al*., 2013a]. By mid-1998, easterlies resumed in the eastern Pacific leading to an increase of equatorial SSS. These SSS changes were caused by the uplift of high-salinity water from below (equatorial upwelling) and the rainfall diminution as the ITCZ moves back north to its original position. The horizontal advection shifted the freshpool (SSS $<$ 35 pss) back to the western part of the basin (west of 170°E).

© 2014. American Geophysical Union. All Rights Reserved.

Figure 5d shows the latitude-time plot of the modeled SSS anomalies (relative to the 2002–2011 period) averaged within 170°E–180°W. The ISAS product does not cover the 1998–1999 La Niña period and could therefore not be used to assess the model. The modeled SSS was however compared to the gridded SSS product described in *Delcroix et al.* [2011] and showed very good agreement (not presented here). From Figures 5c and 5d, modeled SSS anomalies are overall similar in 1998–1999 and 2010–2011, even though the 1998–1999 low-salinity waters (say, SSSA < -0.5 pss) appear later during the year in the equatorial band and move further south.

Similar and dissimilar processes associated with SSS anomalies during the 1998–1999 and 2010–2011 La Niña events have also been investigated from the model outputs. The zonal processes in the western-central Pacific are very similar for the two La Niña phases. This is not the case for the meridional advection. The main difference is in the position of SSS anomalies from the warm pool and SPCZ area, which is mainly governed by the preceding El Niño. Surface forcing is consistent for the two events but shifted south by a few degrees in 1998–1999. The subsurface forcing plays the same role during the two events and inhibits any changes that increase the vertical salinity gradient.

6. Summary and Conclusion

The ENSO cycle is the largest interannual variation of the Earth's climate, and includes a warm El Niño phase and less-documented cold La Niña phase. In this study, we compare and investigate the SSS anomalies captured by different in situ observations, by modeling and for the first time by satellite-derived (SMOS) observations during 2010–2011. During this period the tropical Pacific was in a long La Niña phase following a strong El Niño in 2009. A first La Niña event in 2010 was followed by another event in 2011. Back to back La Niña has been found to be rather common in a recent study [*Hu et al.*, 2013]. It is therefore of interest to study these 2 year events that we call "La Niña phase." We further quantify the responsible mechanisms using a validated DRAKKAR model simulation.

By the end of the 2009 El Niño, all our SSS data sets show a strong bipolar anomaly in the western half of the tropical Pacific, with a negative anomaly in the equatorial band (<-0.8 pss) and a positive anomaly south of about 8°S ($>+0.8$ pss), in agreement with previous studies of El Niño [*Delcroix*, 1998; *Singh et al.*, 2011]. From mid-2010 the equatorial negative anomaly is shifted south together with the southern positive anomaly. A positive anomaly appears near the equator. In 2011, anomalies shift south and amplify except from the one south of 20°S reaching again intensity above 0.8 pss.

The processes associated with these SSS changes were studied from the DRAKKAR simulation output, which also provides all terms of the SSS budget. The analysis of the mixed-layer salinity budget indicates that horizontal advection is the main driver of the modeled SSS changes. Looking at each horizontal advection component, it has been found that the zonal component dominates in the equatorial band and the meridional component farther south. Although important changes in zonal velocity occur at the beginning of 2010, this term does not have such a great impact on SSS changes since strong zonal SSS gradient anomalies rarely coincide. Meridional advection was mainly governed by interannual changes in the meridional SSS gradient associated with the ENSO-related westward and southward displacements of the fresh waters of the warm pool and SPCZ respectively. The (modeled) SSS was also affected by the surface forcing, mainly due to precipitation, which are very much modulated during ENSO in the region of interest. A north-south dipole of surface forcing was in place from mid-2010 to mid-2011. During La Niña the ascending branch of the Walker circulation is at its western-most position causing the suppression of precipitation in the western-central equatorial Pacific (positive E-P anomaly). The high-precipitation zone associated with the very active SPCZ shifts back south of 8°S (negative E-P anomaly). The subsurface forcing has a damping effect on SSS changes induced mostly by surface forcing but also by horizontal advection.

Studying the similarities and dissimilarities of the 1998–1999 and the 2010–2011 La Niña events in term of SSS showed the importance of the ocean state before La Niña kicks in. The two preceding El Niño events (1997–1998 and 2009–2010) were quite different. Some studies have labeled them "Eastern Pacific" and "Central Pacific" El Niño, respectively, as a reference to the position of their maximum SST anomaly. Equatorial SSS interannual anomalies defined by the preceding El Niño are advected south in the Southern Hemisphere by the meridonal currents during the La Niña event. Equatorial SSS anomalies are therefore crucial

© 2014. American Geophysical Union. All Rights Reserved.

to characterize the La Niña event signature farther to the south. Surface forcing and subsurface processes are analogous in both events.

Finally, it is worth pointing out that the use of complementary data sets such as the ones presented in our study is critical to document the Global Ocean mean state and its variability. The ground breaking satellite-based SSS data derived from SMOS (and also Aquarius/SAC-D, although not examined here) provide a new global source of information to study the ocean. SMOS can in deed capture small-scale features coherent with TSG data, which are not represented by ISAS because of the Argo network 300 km nominal resolution, and the smoothing induced by the objective analysis methodology. This is also described in the Atlantic region (N. Kolodziejczyk et al., SMOS salinity in the subtropical north Atlantic salinity maximum: Part II: Observation of the surface thermohaline horizontal structure and of its seasonal variability, submitted to Journal of Geophysical Research-Oceans, 2013). Such new stream of data however requires proper calibration and validation, in which high-resolution in situ data play a key role. The comparison of SMOS SSS and TSG data also shows the quality degradation in the vicinity of islands. The RMSE of SMOS SSS with respect to TSG SSS is higher in our domain than in the eastern south Pacific, far from islands and large land masses by *Hasson et al*. [2013a] and in the northern Atlantic subtropical region (O. Hernandez et al., SMOS salinity in the subtropical north Atlantic salinity maximum: Part I: Comparison with Aquarius and in situ salinity, submitted to Journal of Geophysical Research-Oceans, 2013). The possible influence of land masses in the SMOS image reconstruction should be further investigated in future studies. The inferred RFI should be better sorted out in next SMOS ESA processing (version 6 in preparation). The evaluation of SMOS data using in situ data should therefore be reassessed in the future. The in situ measurements are also essential to study SSS at higher resolution, in depth and before the satellite launch, as well as for assessing the realism of model simulations. Modeling is on the other hand essential not only to examine and quantify processes behind the observed SSS variability but also to study changes at time scale longer than interannual as for instance, decadal variability and global change. An optimal combination of all these data sets into a "well-thought" merged product (maybe using data assimilation) would definitely be of use.

Acknowledgments

This work is a contribution to the ESA GLOSCAL SMOS Cal/Val project. It is supported by CNES/TOSCA SMOS-Ocean, by ESA SMOS+SOS projects, and by the Spanish project AYA2012-39356-C05-03. We benefited from numerous data sets made freely available, including those from the French SSS Observation Service (www.legos.obs-mip.fr/observations/sss) and from the DRAKKAR model group (www.drakkar-ocean.eu). The in situ Analysis System (ISAS) was developed by LPO (CNRS/IFREMER/IRD/UBO) and products were made available by F. Gaillard (wwz.ifremer.fr/lpo/La-recherche/Projets-en-cours/GLOSCAL). The LOCEAN_v2013 SSS maps have been produced by LOCEAN/IPSL (UMR CNRS/UPMC/IRD/MNHN) laboratory which participates in the Ocean Salinity Expertise Center (CECOS) of Centre Aval de Traitement des Donnees SMOS (CATDS) at IFREMER, Plouzané, France (http://www.catds.fr/Products). NOAA_OI_SST_V2 data were provided by the NOAA/OAR/ERSL PSD, Boulder, Colordao, USA (http://www.esrl.noaa.gov/psd/). The programming support of N. Martin and O. Hernandez from LOCEAN in Paris regarding the SMOS data was deeply appreciated. We are thankful to the reviewers for their thoughtful comments, which greatly increased the quality of the present paper.

References

Bosc, C., T. Delcroix, and C. Maes (2009), Barrier layer variability in the western Pacific warm pool from 2000 to 2007, *J. Geophys. Res.*, *114*, C06023, doi:10.1029/2008JC005187.

Boutin, J., N. Martin, X. Yin, J. Font, N. Reul, and P. Spurgeon (2012), First assessment of SMOS data over open ocean: Part II—Sea surface salinity, *IEEE Trans. Geosci. Remote Sens.*, *50*(5), 1662–1675, doi:10.1109/tgrs.2012.2184546.

Boutin, J., N. Martin, G. Reverdin, X. Yin, and F. Gaillard (2013), Sea surface freshening inferred from SMOS and ARGO salinity: Impact of rain, *Ocean Sci.*, *9*(1), 183–192, doi:10.5194/os-9-183-2013.

Clarke, A. J. (2008), *An Introduction to the Dynamics of El Niño & the Southern Oscillation*, Elsevier Sci., 324 pp., London.

Cole, J. E., J. T. Overpeck, and E. R. Cook (2002), Multiyear La Niña events and persistent drought in the contiguous United States, *Geophys. Res. Lett.*, *29*(13), doi:10.1029/2001GL013561.

Delcroix, T. (1998), Observed surface oceanic and atmospheric variability in the tropical Pacific at seasonal and ENSO timescales: A tentative overview, *J. Geophys. Res.*, *103*(C9), 18,611–18,633, doi:10.1029/98JC00814.

Delcroix, T., and C. Hénin (1989), Mechanisms of subsurface thermal structure and sea-surface thermohaline variabilities in the southwestern tropical Pacific during 1975-85, *J. Mar. Res.*, *47*(4), 777–812, doi:10.1357/002224089785076046.

Delcroix, T., and C. Hénin (1991), Seasonal and interannual variations of sea surface salinity in the Tropical Pacific Ocean, *J. Geophys. Res.*, *96*(C12), 22,135–22,150.

Delcroix, T., and J. Picaut (1998), Zonal displacement of the western equatorial Pacific "fresh pool", *J. Geophys. Res.*, Oceans, *103*, 1087–1098, doi:10.1029/97jc01912.

Delcroix, T., and M. McPhaden (2002), Interannual sea surface salinity and temperature changes in the western Pacific warm pool during 1992–2000, *J. Geophys. Res.*, *107*(C12), 8002, doi:10.1029/2001JC000862.

Delcroix, T., G. Alory, S. Cravatte, T. Correge, and M. J. McPhaden (2011), A gridded sea surface salinity data set for the tropical Pacific with sample applications (1950–2008), *Deep Sea Res., Part I*, *58*(1), 38–48, doi:10.1016/j.dsr.2010.11.002.

Font, J., A. Camps, A. Borges, M. Martin-Neira, J. Boutin, N. Reul, Y. H. Kerr, A. Hahne, and S. Mecklenburg (2010), SMOS: The challenging sea surface salinity measurement from space, *Proc. IEEE*, *98*(5), 649–655, doi:10.1109/jproc.2009.2033096.

Gaillard, F. (2012), ISAS-Tool Version 6: Method and configuration, Ifremer, 18 pp., France, doi:10.13155/22583.

Gaillard, F., E. Autret, V. Thierry, P. Galaup, C. Coatanoan, and T. Loubrieu (2009), Quality control of large Argo datasets, *J. Atmos. Oceanic Technol.*, *26*(2), 337–351, doi:10.1175/2008jtecho552.1.

Gouriou, Y., and T. Delcroix (2002), Seasonal and ENSO variations of sea surface salinity and temperature in the South Pacific Convergence Zone during 1976–2000, *J. Geophys. Res.*, *107*(C12), 8011, doi:10.1029/2001JC000830.

Henin, C., and J. Grelet (1996), A merchant ship thermo-salinograph network in the Pacific Ocean, *Deep Sea Res., Part I-Oceanographic Research Papers, 43*(11–12), 1833–1855, doi:10.1016/s0967-0637(96)00084-2.

Hasson, A. E. A., T. Delcroix, and R. Dussin (2013b), An assessment of the mixed layer salinity budget in the tropical Pacific Ocean. Observations and modelling (1990–2009), *Ocean Dyn.*, *63*(2-3), 179–194, doi:10.1007/s10236-013-0596-2.

Hénocq, C., J. Boutin, F. Petitcolin, G. Reverdin, S. Arnault, and P. Lattes (2010), Vertical variability of near-surface salinity in the tropics: Consequences for L-band radiometer calibration and validation, *J. Atmos. Oceanic Technol.*, *27*(1), 192–209, doi:10.1175/2009jtecho670.1.

© 2014. American Geophysical Union. All Rights Reserved.

Hu, Z. Z., A. Kumar, Y. Xue, and B. Jha (2013), Why were some La Niñas followed by another La Niña, *Clim. Dyn.*, *42*(3–4), 1029–1042, doi:10.1007:s00382-013-1917-3.
Kerr, Y. H., et al. (2010), The SMOS mission: A new tool for monitoring key elements of the global water cycle, *Proc. IEEE*, *98*(5), 666–687, doi:10.1109/jproc.2010.2043032.
Kim, W., S.-W. Yeh, J.-H. Kim, J.-S. Kug, and M. Kwon (2011), The unique 2009–2010 El Niño event: A fast phase transition of warm pool El Niño to La Niña, *Geophys. Res. Lett.*, *38*, L15809, doi:10.1029/2011GL048521.
Kripalani, R. H., and A. Kulkarni (1997), Rainfall variability over south-east Asia—Connections with Indian monsoon and ENSO extremes: New perspectives, *Int. J. Climatol.*, *17*(11), 1155–1168, doi:10.1002/(sici)1097-0088(199709)17:11<1155::aid-joc188>3.0.CO;2-B.
Lukas, R., and E. Lindstrom (1991), The mixed layer of the western equatorial Pacific Ocean, *J. Geophys. Res.*, *96*(S01), 3343–3357.
Madec, G. (2008), *NEMO Ocean Engine*, edited, pp. 300, Inst. Pierre-Simon Laplace, France.
Maes, C., J. Picaut, and S. Belamari (2002), Salinity barrier layer and onset of El Niño in a Pacific coupled model, *Geophys. Res. Lett.*, *29*(24), 2206, doi:10.1029/2002GL016029.
Nicholson, S. E., and J. C. Selato (2000), The influence of La Niña on African rainfall, *Int. J. Climatol.*, *20*(14), 1761–1776, doi:10.1002/1097-0088(20001130)20:14<1761::aid-joc580>3.0.co;2-w.
Philander, S. (1989), *El Niño, La Niña, and the Southern Oscillation*, Elsevier Sci., 293 pp., London.
Philander, S. G. H. (1985), El-Niño and La-Niña, *J. Atmos. Sci.*, *42*(23), 2652–2662, doi:10.1175/1520-0469(1985)042<2652:enaln>2.0.co;2.
Picaut, J., M. Ioualalen, T. Delcroix, F. Masia, R. Murtugudde, and J. Vialard (2001), The oceanic zone of convergence on the eastern edge of the Pacific warm pool: A synthesis of results and implications for El Niño-Southern Oscillation and biogeochemical phenomena, *J. Geophys. Res.*, *106*(C2), 2363–2386.
Rasmusson, E. M., and T. H. Carpenter (1982), Variations in the tropical sea-surface temperature and surface wind fields associated with the southern oscillation El Niño, *Mon. Weather Rev.*, *110*(5), 354–384, doi:10.1175/1520-0493(1982)110<0354:vitsst>2.0.co;2.
Reynolds, R. W., N. A. Rayner, T. M. Smith, D. C. Stokes, and W. Q. Wang (2002), An improved *in situ* and satellite SST analysis for climate, *J. Clim.*, *15*(13), 1609–1625, doi:10.1175/1520-0442(2002)015<1609:aiisas>2.0.co;2.
Roemmich, D., and W. B. Owens (2000), The Argo project: Global ocean observations for understanding and prediction of climate variability, *Oceanography*, *13*(2), 45–50, doi:10.5670/oceanog.2000.33.
Ropelewski, C. F., and M. S. Halpert (1996), Quantifying Southern Oscillation—Precipitation relationships, *J. Clim.*, *9*(5), 1043–1059, doi:10.1175/1520-0442(1996)009<1043:qsopr>2.0.co;2.
Sarachik, E. S., and M. A. Cane (2010), *The El Niño-Southern Oscillation Phenomenon*, 369 pp., Cambridge Univ. Press, Cambridge, U. K.
Singh, A., T. Delcroix, and S. Cravatte (2011), Contrasting the flavors of El Niño-Southern Oscillation using sea surface salinity observations, *J. Geophys. Res.*, *116*, C06016, doi:10.1029/2010JC006862.
Trenberth, K. E., G. W. Branstator, D. Karoly, A. Kumar, N.-C. Lau, and C. Ropelewski (1998), Progress during TOGA in understanding and modeling global teleconnections associated with tropical sea surface temperatures, *J. Geophys. Res.*, *103*(C7), 14,291–14,324, doi:10.1029/97JC01444.
Vergely, J.-L., F. Rouffi, P. Waldtefeul, E. Anterrieu, and I. Corbella (2013), SMOS+ Innovation: Polarimetry product validation report. ACGRIST, Sophia-Antipolis, France. [Available at http://smosp.acri.fr/docs/vr.pdf.]
Vialard, J., and P. Delecluse (1998a), An OGCM study for the TOGA decade, Part I: Role of salinity in the physics of the western Pacific fresh pool, *J. Phys. Ocean.*, *28*(6), 1071-1088, doi:10.1175/1520-0485(1998)028<1071:aosftt>2.0.co;2.
Vialard, J., and P. Delecluse (1998b), An OGCM study for the TOGA decade, Part II: Barrier-layer formation and variability, *J. Phys. Ocean.*, *28*(6), 1089–1106, doi:10.1175/1520-0485(1998)028<1089:aosftt>2.0.co;2.
Vialard, J., C. Menkes, J. P. Boulanger, P. Delecluse, E. Guilyardi, M. J. McPhaden, and G. Madec (2001), A model study of oceanic mechanisms affecting equatorial Pacific sea surface temperature during the 1997–98 El Nino, *J. Phys. Ocean.*, *31*(7), 1649–1675, doi:10.1175/1520-0485(2001)031<1649:amsoom>2.0.co;2.
Vialard, J. M., P. Delecluse, and C. Menkes (2002), A modeling study of salinity variability and its effects in the tropical Pacific Ocean during the 1993–1999 period, *J. Geophys. Res.*, *107*, doi:10.1029/2000jc000758.
Yin, X., J. Boutin, and P. Spurgeon (2013), Analysis of biases between measured and simulated SMOS brightness temperature over ocean, *IEEE J. Selec. Top. Appl. Earth Obs. Remote Sens.*, *6*(3), 1341–1350, doi:10.1109/JSTARS.2013.2252602.

© 2014. American Geophysical Union. All Rights Reserved.